3D-Printing polymer-based permanent magnets

R. Domingo-Roca*, J. C. Jackson and J. F. C. Windmill

*Corresponding author. E-mail: roger.domingo-roca@strath.ac.uk (R. Domingo-Roca)

Centre for Ultrasonic Engineering, Dept. of Electronic & Electrical Engineering, Technology and Innovation Centre, University of Strathclyde, Glasgow, G1 1RD, Scotland, United Kingdom

ABSTRACT | Production of permanent magnets is a complex process that implies very specific machinery able to perform very specific actions. Even though this problem has been approached by extrusion-based three-dimensional printing techniques, the resulting parts either have not been fully characterized or present low-resolution outputs. In this study we use the stereolithography three-dimensional printing technique to address this problem and demonstrate that it is possible to develop high-resolution polymer-based permanent magnets. We report an in-depth magnetic characterization of the produced materials, including magnetization of saturation, coercivity, magnetic relative permeability, magnetic behaviour, type of interaction between particles, and magnetic domain orientation. We have further demonstrated that this orientation can be re-arranged. Obtaining contrasting properties of the developed materials opens the possibility of developing personalized, high-resolution devices that can be used in a wide range of fields such as micro-robotics, biotechnology, biomedicine, and medical science among many others.

KEYWORDS: 3D-printing; Polymer-based; Magnetic composites

I. HIGHLIGHTS

- 3D-printing polymer-based permanent magnets is presented.
- High-resolution devices can be developed with an accuracy of 50 microns.
- Development of 3D-printed magnets with different magnetic properties has been demonstrated.
- Such materials can be combined to fulfil user needs depending on the application.

II. INTRODUCTION

Manufacturing processes used to develop permanent magnets are time-consuming as well as demanding very specific and complex machinery to perform complicated processes such as the application of exceptionally high pressures, temperatures, and magnetic fields. Furthermore, these manufacturing processes generate by-products and hazardous waste, making the whole process environmentally unfriendly. However, the main advantage of these process techniques is that the magnets produced using such approaches have extremely large magnetic fields, reaching values up to 1.7 T [1]. One of the paths to overcome such an issue is the use of micro-needles to 3D-print magnetorheological (MR) elastomers (MRE) using the extrusion technique [2-4], more commonly known as fused deposition modelling (FDM) or fused filament fabrication (FFF). Extrusion techniques fabricate parts by melting a filament and extruding it in a layer by layer approach. FDM and FFF approximations heat up thermoplastic materials that are then used to form continuous profiles. Extrusion is one of the most common strategies to 3D-print materials,

and even though it presents some advantages over other 3D-printing techniques, it presents two particular inconveniences: (i) the weight of the extruder and its constant movement onto the part in construction can lead to overshoot, backlash, and banding of the sample, and (ii) the extruder's size directly determines the resolution of the 3D-printed parts. These factors have a direct impact on the resolution limitations of the 3D-printed parts, irrespectively of the material used. Bastola *et al.* demonstrated that this technique can be used to 3D-print iron powder-based MRE where the mechanical properties can be controlled by the application of an external magnetic field [2]. Other researchers have also used the extrusion 3D-printing technique to further investigate the possibilities of developing different arrays of MRE materials under an external magnetic field [3] for different purposes such as bio-signal monitoring [4]. Even though these studies seem to open the doors of developing magnetic 3D-printable materials they do not report the magnetic characterization of the produced MR samples, meaning that there is no clear understanding of what the applications of such materials could be in a broader approach. This gap was filled by Khazodian *et al.* in their study of the development of MRE using recycled Sm-Co powder, revealing the possibility to extrude MRE with hard-magnet properties and therefore meaning that these composites could be potentially used in data storage systems or as small generators, among many others. Notwithstanding that work, which uniquely presented the coercivity and remanence analysis of the materials as a function of the filler content, the study still did not prove if it was possible to 3D-print magnets with high-resolution in specific shapes. The resolution to this problem is found by changing the 3D-printing strategy and using digital light processing (DLP) stereolithography apparatus (SLA), based in the photo-polymerization process by which an ultraviolet (UV) light source forces the molecules of the polymer chains to link to each other. This process is assisted by computer-aided design (CAD) files, which are sectioned in slices of specific resolution and projected on the surface of the resin. The UV light (or, alternatively, a laser) is then applied into each one of these slices for a certain amount of time until the polymer solidifies through photo-chemical processes, acquiring the shape of the projected cross-section (Fig. 1). The DLP-SLA approach was used by Lu *et al.* to develop iron-based MR materials embedding Fe nanoparticles (NPs) of 20 microns in high weight concentrations (higher than 70 % in weight, wt%) and 3D-printing slices of 200 microns thickness [5]. The authors combined this production process with the application of an external magnetic field in order to induce the motion of the NPs to specific locations of the 3D-printed part, a smart technique allowing the development of polymer-based systems with specific functional parts. Nevertheless, the authors found that the distribution of magnetic NPs was not completely homogeneous after the 3D-printing process, a phenomenon that may be a big issue when developing sensors for specific applications that need to generate or detect uniform magnetic fields.

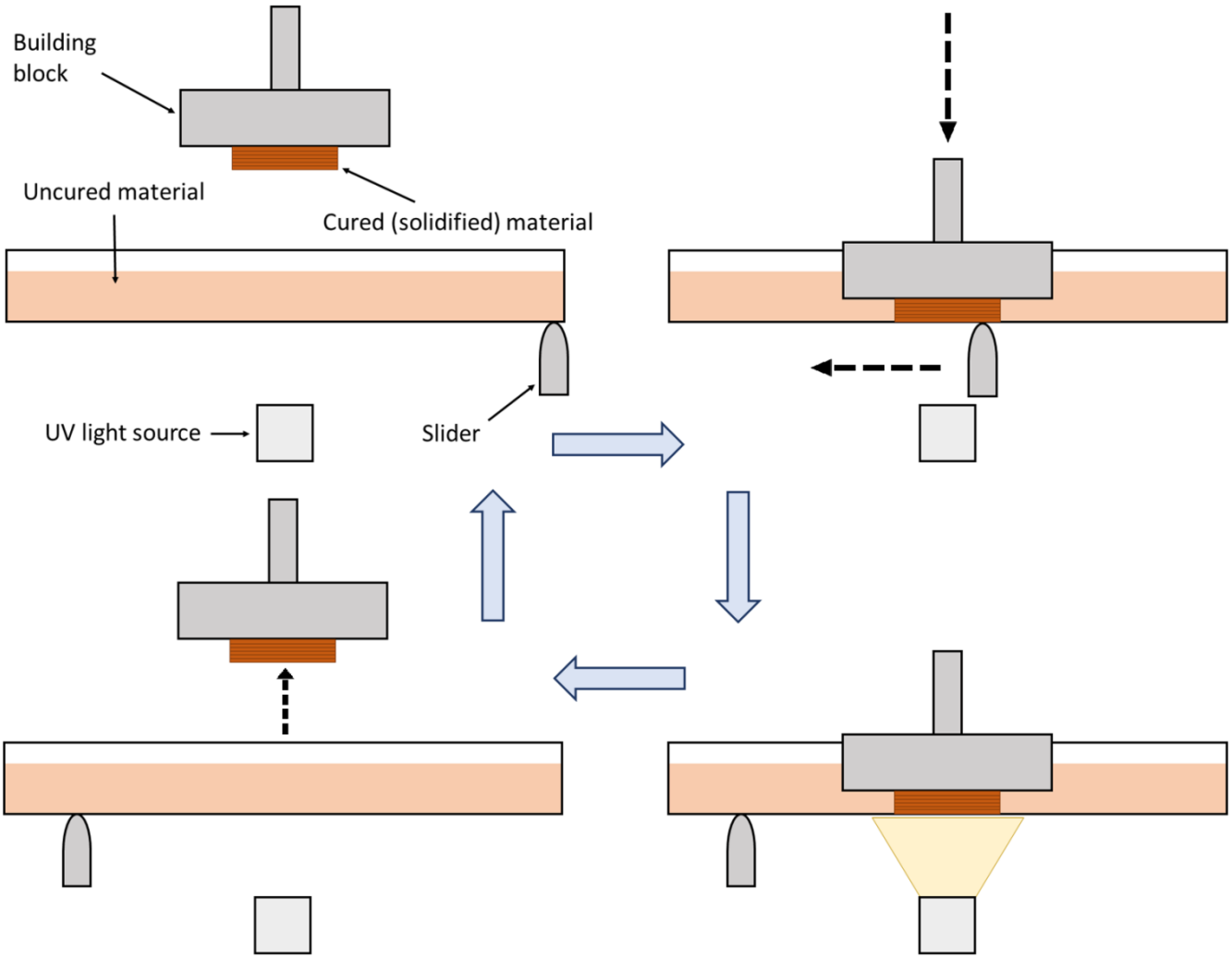

Fig. 1: Illustration of the DLP-SLA process. The top-left image shows the starting point of the process. The building block (or holder) moves down until it contacts the membrane where the uncured polymer lies. After contact is made, the slider applies the first slice (cross-section) of the part and removes the excess polymer (top-right). The UV light (or, alternatively, a laser light) is applied for a certain amount of time to produce photo-chemical linkage of the polymer, resulting in its solidification into the building block (bottom-right). Finally, the holder is removed and the slider returns to its initial position (bottom-left). The process is repeated layer-by-layer until the full part is produced.

The aim of this work is to assess the fabrication limitations previously stated by using the DLP-SLA 3D-printing approach, as it permits the production of parts in a higher resolution and with finer and smoother finish, better functional surface quality, and more complex shapes. These are not the unique advantages of using this 3D-printing technique, as it also allows the development of several composite magnetic materials with very contrasting mechanical and magnetic properties by simply changing the build material during the print. These materials can be combined in one print in different geometries and distributions in order to suit the manufacturer's needs. Furthermore, using DLP-SLA 3D-printing technology allows production in a more personalized, time-efficient, and environmentally-friendly manner.

Iron (II, III) oxide, commonly known as magnetite (Fe_3O_4), is the most magnetic of all natural minerals. It crystallises with a cubic inverse spinel structure at room temperature [6], and it presents ferrimagnetic behaviour in its bulk form with a Curie temperature of 858 K. When cooled down, magnetite undergoes a crystal structure phase transition to a monoclinic crystal lattice in which its magnetic, electrical, and thermal properties are modified [7]. This crystal structure phase transition, which takes place around 120

K, is known as the Verwey transition and it is dependent on domain-state, grain size, and iron-oxygen stoichiometry [8]. Due to finite size effects, this bulk ferrimagnetic behaviour disappears when working with magnetite nanoparticles (NPs), which present a superparamagnetic behaviour below a specific size [9-11], making it suitable for applications in chemistry [12, 13], medical diagnosis [14, 15], and storage devices [16, 17], among many others. Magnetite has been found to be present in some animals and bacteria [18, 19], in human brain tissue [20], where it is thought to play a role in long-term memory [21], and in various igneous rocks [6]. Magnetite is used over other highly magnetic materials, such as cobalt or nickel, because both the latter elements are remarkably toxic and present an electronic configuration that easily yields to oxidation.

One important feature that must be taken into consideration when working with magnetic NPs is their size, as it plays a key role in the final magnetic properties. Working with large NP sizes implies that there exist several magnetic domains within the particle, making the inversion of magnetization happen through the movement of the walls of the domains rather than spin rotation, resulting in low values of coercive field, H_c, (see Fig. 2). When the NPs size is reduced they become single domain, and thus the inversion of magnetization happens via *coherent rotation*, which has a high energetic cost and leads to an increase of the coercive field. Otherwise, if the size of the NPs is too small, thermal agitation is non-negligible and provokes fluctuations and, therefore, H_c decreases again becoming eventually zero (*i.e.,* transition from ferromagnetic to superparamagnetic, as shown in Fig. 2). When embedding magnetic NPs within a polymeric matrix, their concentration will not only have a direct effect on the magnetization of saturation, which will increase as a function of the content of magnetic material, but will also have an influence on the coercive field of the resulting composite; if NPs are very close to each other, dipole-dipole interactions will occur. Furthermore, when decreasing the NP size, the effective magnetic anisotropy energy densities increase, resulting in an increase of surface anisotropy and causing an increase of H_c at low temperatures [18, 19]. Therefore, in general, a high concentration of magnetic material implies a low coercive field due to an increase of such interactions.

In composite magnetic materials, even though H_c depends on both the NPs size and concentration, the magnetization of saturation, M_s, remains approximately constant at room temperature [18] indicating the non-negligible existence of dipolar interactions between them when embedded within a matrix. Nevertheless, at low temperatures (near 0 K) the increase of anisotropy results in an increase of the coercive field when working with superparamagnetic NPs [22]. Hence, these magnetic properties can be adequately tuned by changing the size, type, and concentration of the filler, as well as they will determine the type of magnetic behaviour the resulting composite will present (superparamagnetic, ferromagnetic, antiferromagnetic…). Furthermore, tuning these properties will have a direct impact on other magnetic properties of the composite such as its relative permeability and, therefore, its magnetic susceptibility, highly relevant depending on their applicability.

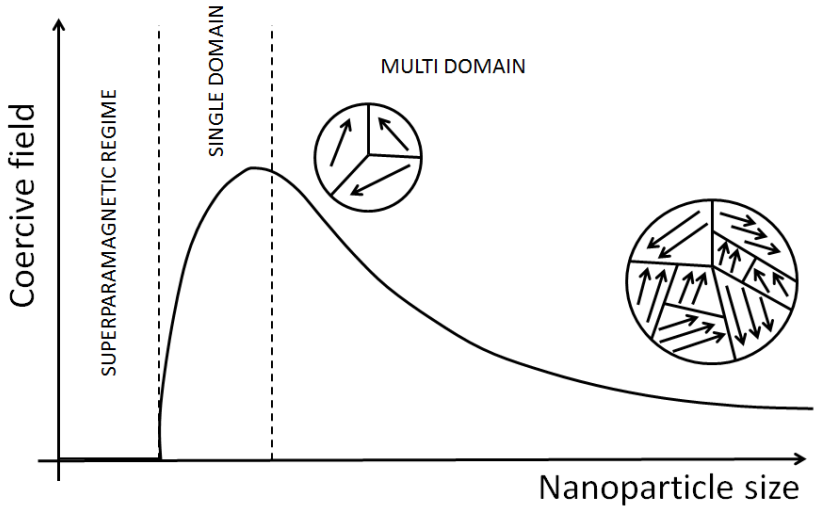

Fig. 2: Diagram of the relationship between coercive field and magnetic NPs size, discerning between single and multi-domain regimes, as well as the superparamagnetic and the ferromagnetic behaviour. Image modified from [24].

In this work, we report on the results of work to high-resolution 3D-printing magnetic materials with contrasting physical properties on the micro-scale and their full magnetic characterization. 3D-printing materials with different magnetic properties at this scale allows their potential use in a wide range of applications such as biomedicine, biotechnology, medical science, and storage devices among many others. Furthermore, we investigate the possibility of using rapid prototyping technology to develop hybrid materials in which different composites presenting distinct magnetic behaviours are added together, accomplishing an exceptional mix of magnetic properties and therefore enhancing their applicability range.

III. MATERIALS AND METHODS

The experiments reported in this article used iron (II, III) oxide (Fe_2O_3) NPs 50-100 nm size, bisphenol-A ethoxylate dimethacrylate (BEMA), poly(ethylene glycol) diacrylate (PEGDA), phenylbis(2,4,6-trimethylbenzoyl)phosphine oxide (Irgacure 819), triarylsulfonium hexafluorophosphate salts mixed 50% in propylene carbonate (TH salts), and SUDAN I (Sigma Aldrich). Iron (Fe) NPs 25 nm size were also used (US Research Nanomaterials Inc.).

A. Synthesis of the polymer matrices

Four different polymeric matrices were developed using liquid polymer and a photo initiator. BEMA is an organic polymerisable methacrylate group linked to bisphenol by oligo-groups of different length, which determines the glass transition temperature of the thermoset networks after exposure to ultraviolet (UV) light. Similarly, PEGDA is a hydrophilic hydrogel in which the cross-linker also acts as a cross-linked chain [25]. Photochemical initiators are used to crosslink unsaturated monomers through the homolysis process, and are a fundamental specie when developing photo-curable 3D-printable materials. Irgacure 819 was added, separately, in both BEMA and PEGDA at 1 wt% and the mixture was left under magnetic stirring for 24 hours. 0.1 wt% of SUDAN I was added into the mixture to improve 3D-printing resolution, as their light-sensitive azobenzene moieties block UV light from

scattering [26], therefore producing better 3D-printing resolution. The same process was repeated replacing Irgacure 819 with TH salts. The polymers containing Irgacure 819 presented a yellowish colour whereas those containing TH salts appeared transparent. When adding SUDAN I to the mixtures both of them became orange.

B. Synthesis of the magnetic composites

UV-light photo-sensible magnetic composites were developed by embedding Fe_3O_4 and Fe NPs within the different polymers at different wt% (25, 50, and 75) using a THINKY AER-250 (Intertronics, Kidlington, England) mechanical mixer, mixing the composite for 3 minutes at 1500 rpm, and de-foaming it for 2 minutes at 1200 rpm. The composites containing Fe_3O_4 NPs exhibited a black colour, whereas those containing Fe NPs revealed a grey tonality. After mechanical mixing, samples of the different magnetic composites were built using the screen printing technique (RK control coater) at a slice thickness resolution of 50 µm as a proof-of-concept. Every layer was cured under UV light for two minutes using an Intertronics IUV250 Hand Lamp (Intertronics, Kidlington, England, UK). The screen printing technique is a rudimentary DLP-SLA approach in which the 3D-printing process is not machined, and it is the user who needs to apply both the material and the UV light independently. The steps to follow are the same as those shown in Fig. 1 but in a non-machined manner. This technique provides several sliders that control the thickness of each layer, allowing for resolutions of 50, 75, 100, 125, and 150 microns. Furthermore, each of these sliders is attached to two height micro controllers that allow to add a few microns to the desired slice, permitting the development of layers of the slider thickness + 9 µm.

A hybrid composite material was also developed by adding layers of Fe_3O_4(50)@Irgacure819+PEGDA and Fe(50)@Irg819+PEGDA together.

Although the screen printing technique was successfully used to develop samples with a high NPs concentration, when using the 3D Printer at these loading percentages aggregation of the magnetic NPs was observed to occur, leading to poor local 3D-printing resolution. Hence, samples with a lower concentration of magnetite were used for 3D-printing (using an ASIGA PicoPlus27 machine, ASIGA, Anaheim Hills, California, USA). The ASIGA machine is a UV-based stereolithography (STL) 3D printer that allows building parts at a minimum slice thickness resolution of 10 microns, creating structures from CAD files in a layer-by-layer manner. The composites containing Fe NPs were not used for 3D-printing due to the special measures that must be taken when working with them, as an exothermic reaction takes place when used at room temperature which, if not properly controlled, may lead to fire. This is a feature that can be properly controlled when screen-printing the materials but not when machining the process using the 3D-printer. Hence, all the Fe-based and hybrid samples were developed using the screen printing approach. Furthermore, when the polymer is cured under UV light it expands, leading to slight variations of the thickness that need to be accounted for when developing the CAD files. Hence, obtaining a good balance between 3D-printing resolution and physical properties is vital

during the fabrication process: whereas higher concentrations of NPs will produce a better magnetic output, this same parameter will lead to poor 3D-printing resolution due to an increase of light scattering and agglomeration of NPs. This is the main reason why we selected the wt% presented in this work.

C. Vibrating sample magnetometer

A vibrating sample magnetometer (VSM) permits an in-depth study of the magnetic properties of materials, providing a recording of the *M-H* hysteresis loops as well as analysis of the change of magnetic moment of the samples (*ΔM*). Whereas the former provide very valorous information about the magnetic material, such as coercivity, remanence, type of magnetic behaviour, and nanoparticle size, the latter provide information about magnetic interactions in particulate media [27-29]. The *ΔM* plot is defined by Eq. (1) [30]. The positive/negative *ΔM*'s are usually interpreted in terms of magnetizing/demagnetizing-like interactions between ferromagnetic particles.

$$\Delta M(H) = m_{rs} - [2m_{IRM}(H) - m_{DCD}(-H)] \tag{1}$$

where $m_{IRM}(H)$ is the magnetic moment of the isothermal remanent magnetization (IRM) process at the corresponding applied *H*, m_{rs} is the remanent saturation magnetic moment, and $m_{DCD}(-H)$ is the magnetic moment on the DC demagnetization (DCD) curve for the value *–H*.

The *M-H* hysteresis loops can be fitted using a Langevin function, as it describes assemblies of particles with freely rotating moments, defining superparamagnetic systems, described by Eq. (2) [27-29].

$$\frac{M}{M_s} = \coth\left(\frac{\mu H}{k_B T}\right) - \frac{k_B T}{\mu H} \tag{2}$$

where M_s is the magnetization of saturation, k_B is the Boltzmann constant, *T* is the temperature, and μ is the magnetic moment, given by $\mu=\pi M_s d^3/6$, being *d* the particle's diameter. Thus, Eq. (2) becomes:

$$\frac{M}{M_s} = \coth\left(\frac{\pi M_s d^3 H}{6k_B T}\right) - \frac{6k_B T}{\pi M_s d^3 H} \tag{3}$$

Therefore, Eq. (3) can be used to determine the NPs size from the obtained experimental data from the *M-H* curves.

The VSM used to plot the *M-H* curves presented in this study had size limitations of 130 mm in thickness and 8 mm in side length, therefore limiting the shape and size of the composites to be measured.

IV. EXPERIMENTAL RESULTS

A. 3D-printing and morphological analysis

Square samples of 8 mm side length and 0.120±0.010 mm (mean±s.e.) thickness were built to obtain the *M-H* curves. This size was chosen due to the VSM size limitations. Separately, three different samples were 3D-printed: a small square-shaped membrane (5X5 mm) with a thickness of 2.5 mm, and two larger square-shaped membranes (10X10 mm) of 2 mm and 1 mm thickness (see Fig. 3). The small sample was 3D-printed at a 5 wt% of Fe_3O_4@BEMA, whereas the two large samples were 3D-printed at a concentration of 25 wt%. Furthermore, a hollow 10 mm diameter half-sphere with 1 mm diameter holes on its surface was 3D-printed to demonstrate the possibility of high-resolution 3D-printing. The holes are laterally separated by 0.5 mm (see Fig. 4). Finally, the hybrid samples were built following the VSM stipulated size conditions. All the samples were 3D-printed at percentages that ensured the best balance between physical properties and 3D-printing resolution. Even though it has been observed that M_s increases with NP concentration, a higher filler fraction within the polymer implies more light scattering. This feature can be improved when using the screen printing technique, although it also has its limitations. It was noted that whereas using the 3D printer the best resolution was obtained at a 25 wt%, it was possible to produce low-resolution parts at a 50 wt%. The 3D printer allows for the development of smaller and more complex geometries that produce a higher degree of light scattering, meaning that the weight concentration of NPs needs to be reduced in order to obtain the best balance between 3D-printing resolution and magnetic output.

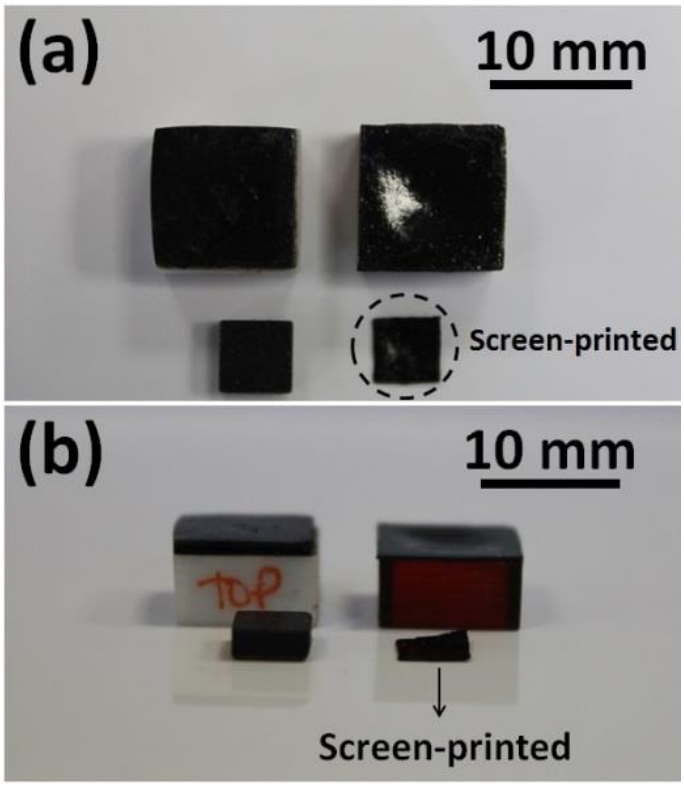

Fig.3: 3D-printed and screen-printed samples. The large samples lie on a 3D-printed support made o commercial 3D-printable materials. (a) and (b) show the top and side view, respectively.

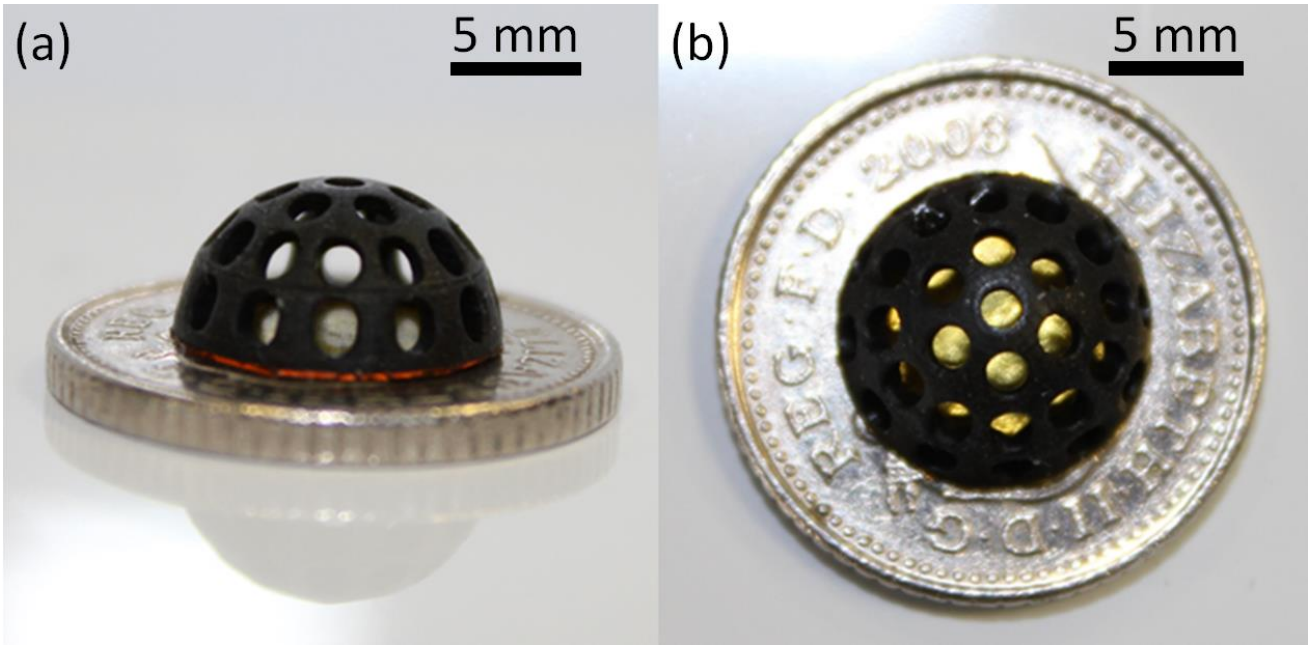

Fig. 4: 3D-printed hollow half-sphere with circular holes on its surface. (a) and (b) show different views of the same part compared with a United Kingdom 5 pence coin. The base diameter is 10 mm and the holes have a 1 mm diameter.

Before analysing the magnetic properties of the 3D-printed and screen printed samples we studied their morphological structure using a scanning electron microscopy (SEM). The obtained images can be seen in Fig. 5.

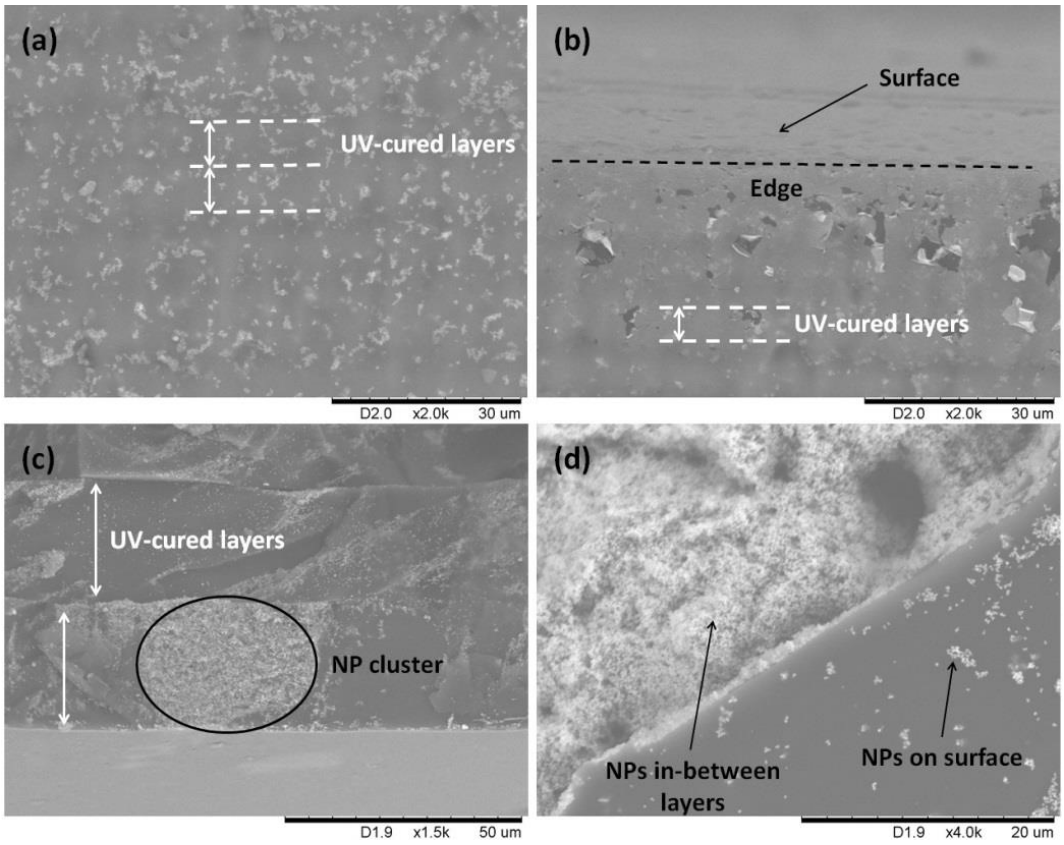

Fig. 5: SEM images of the 3D- and screen-printed magnetic composites. (a) Cross section of one of the 3D-printed magnetic samples in which the 3D-printed layers can be seen, (b) The edge of one of the 3D-printed samples, (c) Cross section of one of the screen printed samples, and (d) One of the screen-printed samples when one of the layers has been removed.

It can be seen from Fig. 5 that there are big structural differences between the 3D-printed and the screen-printed samples. Whereas 3D-printed samples (Fig. 5a and 5b) reveal a better crosslinking between layers due to a low time UV-light exposure for each of them, screen-printed samples show a low degree of crosslinking between layers as every single one of them is fully polymerised. The second main difference is the distribution of NPs within the polymer. Whereas in 3D-printed samples the distribution seems to be more uniform, in screen-printed samples NPs tend to agglomerate more and form big clusters. It was further observed that even though NPs tend to remain in-between layers, some of them accumulate on the surface of each layer (Fig. 5d). The size of the NPs could not be experimentally determined due to the SEM resolution limits. Nevertheless, this is a feature that can be further investigated by using alternatives techniques.

One of the main advantages of using polymers with completely different mechanical properties is the enhancement of the applicability range of these materials: whereas BEMA-based composite materials present an elastic behaviour, PEGDA-based composite materials show a plastic nature [26]. Hence, these materials present very different values of hardness and elastic moduli, which are influenced by both the filler and the UV-light exposure time [26, 34].

B. Magnetic properties: VSM analysis

The *M-H* hysteresis loops of the magnetic composites containing Fe_3O_4 and Fe NPs are shown in Fig. 5, where their contrasting magnetic behaviour can be observed in the close-up image: on one hand, magnetite-based composites presented a ferromagnetic behaviour, whereas on the other hand, Fe-based composites were superparamagnetic. The H_r and M_s values obtained from these curves (see Table 1, SI for details) were measured to be, respectively, within the range of 15 -17 Oe and 87-167 emug/g, and 104-107 Oe and 23-50 emu/g for Fe and magnetite, respectively. Whereas H_c values remain constant with respect to filler concentration, M_s values increase with it. Using these curves, an estimation of the relative permeability of the 3D-printed composites can be obtained, ranging from 1.60 to 3.08 (see Table I, SI for further details).

The hybrid sample was observed to feature the best combination of magnetic properties of each of the individual composite materials, as it reported a high M_s value and the presence of a non-negligible coercive field (see Fig. 1, ES) proving that it is possible to combine composite magnetic materials with distinct magnetic properties in one unique 3D-print with the aim to obtain their adequate combination to suit the desired application.

The *M-H* curves were fitted using Eq. (3) to determine the NPs size of the particulate media. The fitting functions and the NPs sizes determined using the Langevin function can be observed in Fig. 2, SI and Table I, SI, respectively. Two different *d* values were determined in each case; one corresponding to the experimental M_s measured with the VSM, and another one corresponding to the M_s value obtained from the fitting function (top and bottom one, respectively, in Table II, SI) in OriginPro®. It was observed that using the experimental or the fitting M_s value did not present a big difference in determining the NPs size, yielding to

maximum errors of 4.55% when determining *d*. Nevertheless, the average magnetite NPs size was calculated to be 9.34±0.32 nm with a fitting average accuracy of a 99.88% but the size reported by the manufacturer is of 50-100 nm, showing that Eq. (3) does not provide a good approximation to determine *d* of ferromagnetic NPs, but it does provide an accurate estimation of those presenting superparamagnetic behaviour. SEM images of the 3D- and screen-printed magnetic composites can be seen in Fig. 7, suggesting that the small clusters of magnetic NPs reach maximum sizes of a few microns. Nevertheless, this technique does not permit the exact determination of the size of individual NPs as our SEM limitations restrict to a few microns the maximum amplification area. Hence, this needs to be further studied using other measurement techniques.

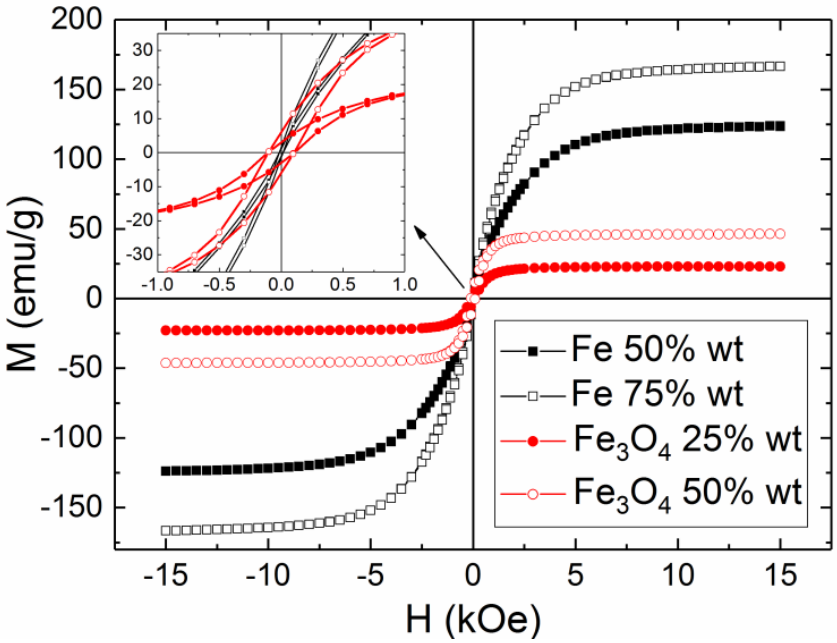

Fig. 6: *M-H h*ysteresis loop plots of the Fe_3O_4 composites at 25 wt% and 50 wt% concentrations, and Fe composites at 50 wt% and 75 wt%. The top-left corner graph shows a close-up look at the low-field regime in which the ferromagnetic and superparamagnetic behaviour of the composites containing Fe_3O_4 and Fe NPs, respectively, can be observed.

In order to fully characterize the magnetic properties of the 3D-printable composite materials, the *ΔM* plots of the ferromagnetic samples were studied (see Fig. 7). These experiments cannot be performed in samples that do not present any effective coercive field. The shape of the *ΔM* curves revealed the presence of a dipolar coupled system in which the interactions attempt to demagnetize the material (*ΔM*<0) [29].

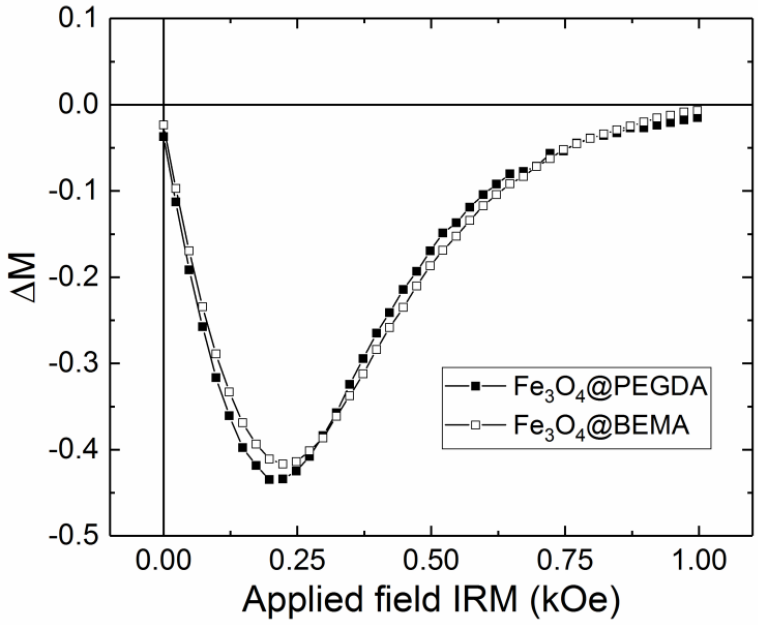

Fig. 7: Change of magnetic moment of the synthesized magnetic composites, ΔM curves for the Fe_3O_4 composite at 50 wt% within PEGDA (solid black squares), and for the Fe_3O_4 composite at 50 wt% within BEMA (empty squares).

As expected, neither the type of polymeric matrix nor the photo-initiator have any impact on the magnetic properties of the composites. Therefore, the NPs type, size, and concentration are the only determining parameters directly influencing M_s. Constant coercive fields were measured when increasing the wt%.

Even though some of the magnetic properties of the 3D-printable composites still need to be optimised, the possibility to 3D-print permanent magnets presents a revolution in the production process, as the magnetic properties of such composites can be finely tuned by adjusting the parameters of the composite materials such as the type, size, and concentration of the filler, thus enhancing their applicability range by working with soft permanent ferromagnetic materials or with superparamagnetic composites. Furthermore, developing sensors through additive manufacturing implies a huge decrease of the production cost, and also the 3D-printing process allows for a high-resolution customization and personalization process to make desired parts adapted to the users' needs. In combination with the complex 3D structure possibilities afforded by 3D printing, there is huge scope for printing complex, small-scale, magnetic structures for a variety of applications.

C. Magnetic properties: magnetic domains analysis

The intensity and orientation of the magnetic domains of the 3D-printed samples was measured using a GM07/GM08 Gaussmeter (Hirst Magnetic Instruments Ltd., Cornwall, United Kingdom) using the set up presented in Fig. 8.

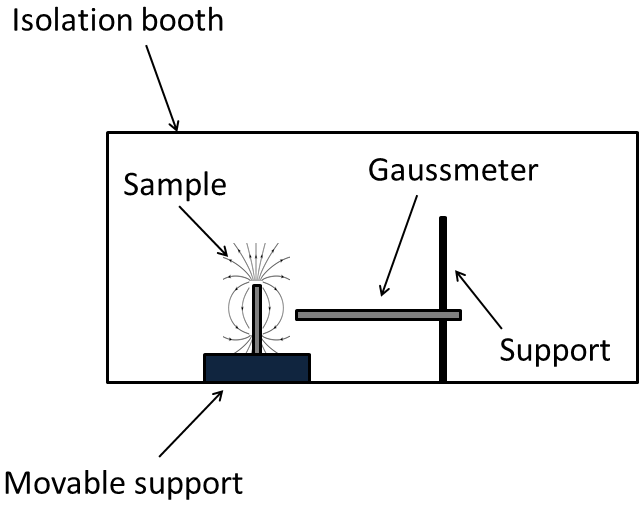

Fig. 8: Sketch of the experimental set up used to measure the magnetic field generated by the 3D-printed samples. The full set up was mounted inside of a magnetically isolated booth to minimize magnetic noise. Nevertheless, magnetic field measurements were taken within the isolation booth without any magnetic samples to measure the background magnetic field.

All the samples presented a permanent magnetic field in which the magnetic domains were observed to be randomly distributed (see Fig. 9a). Thus, poling of the samples was needed to provide them with a good N/S distribution of the magnetic domains, which was achieved by placing the samples in between two NdFeB magnets during 2 hours at 150° C. The magnetic field generated by the poling magnets is shown in Fig. 9b and the magnetic field generated by the 3D-printed samples after magnetic poling is shown in Fig. 10. In both cases the generated magnetic field has been normalised with the background magnetic field, which includes components from equipment present in the laboratory (*i.e.* oscilloscopes, microphones, and computers) as well as a component arising from the Earth's magnetic field. The background magnetic field was measured to be 0.089 mT.

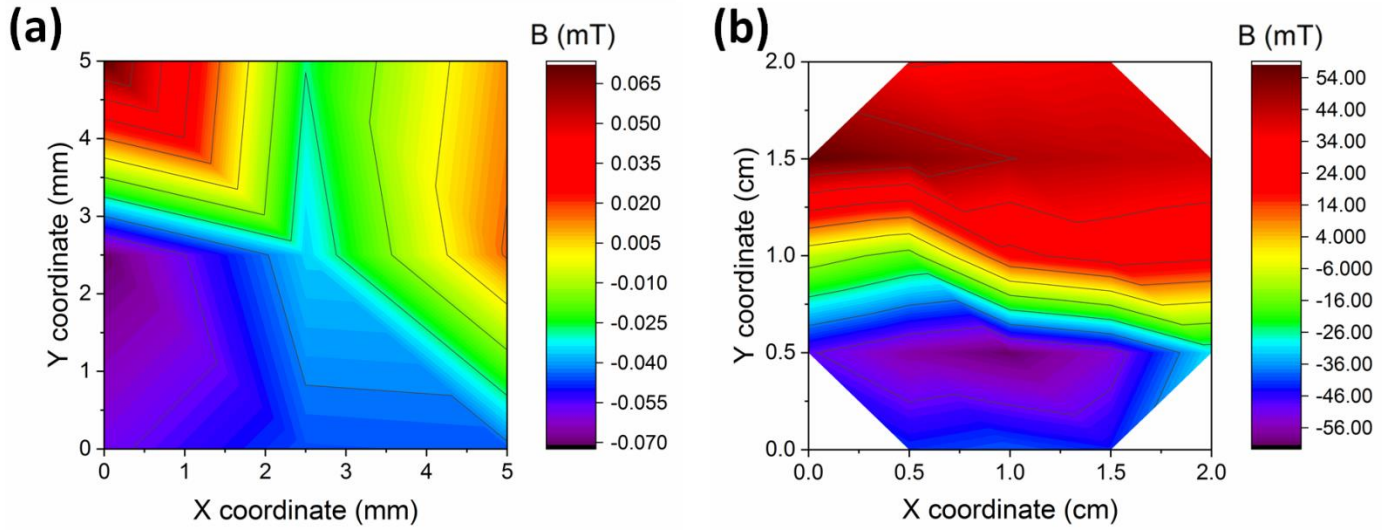

Fig. 9: (a) Surface plot of the orientation and intensity of the measured magnetic field of the magnetic domains of the small non-poled 3D-printed sample. (b) **S**urface plot of the orientation and intensity of the measured magnetic field of the magnetic domains of the NdFeB magnet.

It was noted that the direction of the magnetic domains after poling depends on their position during such a process, as the N/S poles of the 3D-printed samples are not completely symmetric (Fig. 10). Hence, it is possible to optimize the magnetic field of the 3D-printed samples by locating them at specific positions of the NdFeB magnets during the poling process. Nevertheless, all the samples presented permanent magnetization reaching maximum values of magnetic field of 1.025 mT.

Fig. 10 shows that even though the polarity of the 3D-printed magnets is well-defined, the field intensity is not completely uniform in two of the samples. This is associated with the non-uniform distribution of the NPs within the polymeric matrix, as well as to aggregation of NPs. Agglomeration of NPs has been shown to diminish through the use of more viscous fluids as polymer matrices, as well as the use of surfactants, which play a key role in reducing the Van der Waals forces that cause agglomeration [35, 36]. It must also be taken into consideration that when working with magnetic NPs Van der Waals forces are not the only forces involved in the formation of NPs clusters, but also that the magnetic forces between the NPs are involved, which might make the process to reach a more uniform NPs distribution more complicated.

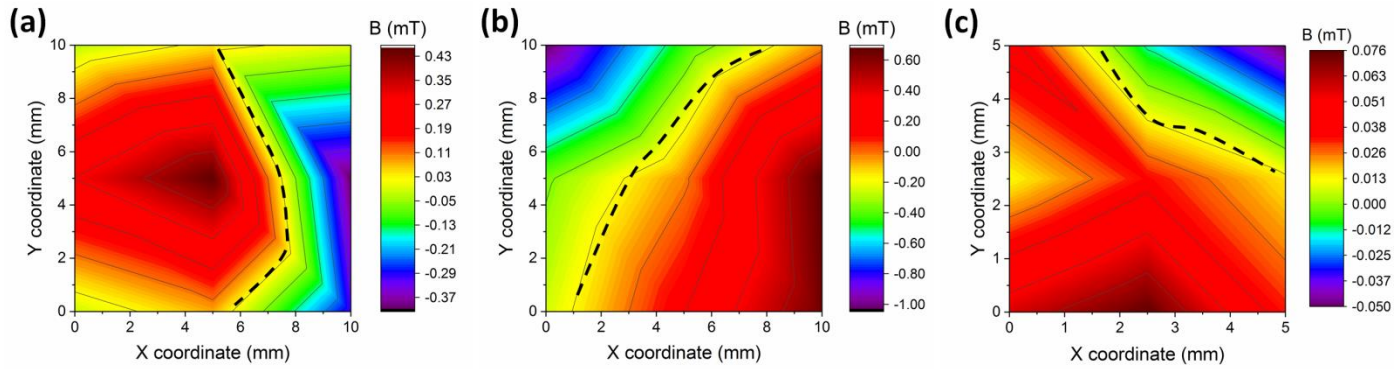

Fig. 10: Experimental plot of the magnetic field orientation and intensity after magnetic poling of (a) the 3D-printed big square thick, (b) 3D-printed big square thin, and (c) 3D-printed small square samples. The dashed lines represent the change of polarity of the samples (N/S) due to the poling magnet having a spatially varying magnetic field distribution. Note the larger scale ranges in comparison to Fig. 8.

It must be noted that both size and thickness of the 3D-printed samples generate different magnetic fields. The larger the 3D-printed sample is, the higher magnetic field it generates. The 10 mm side length sample of 1 mm thickness (Fig. 10a) generated a magnetic field lower than that generated by the sample of the same side-length and twice its thickness (Fig. 10 b), associated to higher content of magnetic material. On the other hand, it was observed that reducing the side length to 5 mm and increasing the thickness to 2.5 mm, the magnetic field was reduced by a factor 10, associated with the reduction of magnetic material due to the decrease of the sample's volume. Hence, the produced magnetic field was observed to be strongly reliant on the shape and size of the 3D-printed samples, becoming a feature that needs to be further characterized in distinct geometries and sizes.

After magnetic poling, all the 3D-printed samples presented a well-defined N/S orientation of the magnetic domains in accordance with that of the poling magnet. Nevertheless, it was observed that small changes in the location of the 3D-printed samples onto

the poling system lead to non-symmetric N/S magnetic polarization, which needs to be finely controlled, specially if 3D-printing nano- and micro-devices. Furthermore, the non-homogeneous distribution of the magnetic NPs can also be observed after the poling process, as the magnetic field generated by the sample is not uniform within the same magnetic pole of the 3D-printed sample. This, though, could be a consequence of the non-uniformity of the intensity of the magnetic field created by the poling magnet.

Finally, it must be noted that all the magnetic 3D-printed composites are polymer-based materials consisting of long EO chains. The structure and arrangement of these chains determine the glass transition temperature. Even though the poling process was performed at 120^{o} C and no macroscopic changes of the geometry and structure of the samples was observed, the polymers may have experienced microscopic changes in their structure, a feature that needs to be further studied.

V. CONCLUSIONS

In this work we report a simple way to develop 3D-printable permanent polymer-based magnets using the DLP-SLA 3D-printing approach. We also present the possibility to 3D-print polymer-based magnetic materials with very contrasting physical properties that can be further combined in one unique print. This properties' tuning of the composite materials allow for a high degree of tunability of the resulting parts, making them suit the desired applications filed.

Irrespective of the type and size of filler, the highest and lowest M_s values were measured at the highest and lowest wt%, respectively, where the non-homogeneous distribution of the NPs within the polymeric matrix play an important role. Inversely, the H_c values were observed to be independent of the NPs concentration and distribution, presenting larger values in magnetite-based composites, therefore suggesting that H_c values rely on the NPs size. The hybrid material presented a good combination of the aforementioned properties, even though further investigation needs to be done to optimise its response. The ΔM analysis revealed the presence of a dipolar coupled system in which the interactions between the magnetic domains tend to demagnetize the material, a phenomenon arising from anisotropy effects. The relative permeability values were determined to be within the range of 1.60-3.08, depending on both the filler type and concentration.

The size of the NPs was theoretically determined by fitting the *M-H* hysteresis loops using a Langevin function, which confirmed the superparamagnetic behaviour of the Fe-based composites. It was noted that the calculated size of the Fe_3O_4-based composites did not match that reported by the manufacturer, suggesting that the Langevin function provides a good explanation of superparamagnetic systems, but does not work as well for those materials presenting a different magnetic behaviour. SEM images suggest agglomeration size of a few microns, but this technique did permit an exact determination of the NPs size.

The 3D-printed materials were measured to be soft permanent magnets with randomly oriented magnetic domains, as expected after an STL process under normal conditions. In this study we have proved that it is possible to re-arrange the orientation of the magnetic domains by using a simple poling process using a NdFeB permanent magnet with a well-defined polarity. Under this set up, the magnetic domains of the 3D-printed samples align with the field lines of the NdFeB magnet. Analogously to what happens in a piezoelectric poling process, the intensity and duration of the external applied field has been observed to have no influence in the magnetic properties of the 3D-printed samples, only re-arranging the direction of their magnetic domains.

Hence, using the STL 3D-printing approach presents a great opportunity to produce polymer-based magnets with contrasting physical properties, as they may be of use in a variety of different fields that are in the zenith of their development, mainly in biotechnology, biomedicine and medical science, for example. Furthermore, specific micro- and nano-systems that can be manipulated using external magnetic fields can also be developed in an easy and personalized way through additive manufacturing processes, allowing for applications in information storage, computer science, acoustic and non-acoustic pressure sensors, or the development of transformers amongst many other applications.

VI. ACKNOWLEDGEMENTS

The authors would like to thank Prof. Thomas Thomson and Dr. Alex Lincoln for the help provided to write this paper, as well access to their facilities at the University of Manchester. We also want to thank Prof. Jordi Sort from the Universitat Autònoma de Barcelona for the useful conversations about magnetic properties of composites.

This research was supported by the European Research Council (ERC Grant Agreement n. 615030) under the European Unions' Seventh Framework Programme (FP/2007-2013).

Data availability

The raw/processed data required to reproduce these findings cannot be shared at this time as the data also forms part of an ongoing study.

REFERENCES

[1] P. Campbell, **Permanent Magnet Materials and Their Application**. Cambridge University Press. 1996.

[2] A. K. Bastola, V. T. Hoang, L. Li, **A novel hybrid magnetorheological elastomer developed by 3D printing**, Mater. Des., 114 (2017), pp. 391-397.

[3] Z. Chen, L. Ren, J. Li, L.Yao, Y. Chen, B. Liu, L. Jiang, **Rapid fabrication of microneedles using magnetorheological drawing lithography**, Acta Biomaterialia, 65 (2018), pp. 283-291.

[4] L. Ren, Q. Jiang, Z. Chen, K. Chen, S. Xu, J. Gao, L. Jiang, **Flexible microneedle array electrode using magnetorheological drawing lithography for bio-signal monitoring**, Sens. Actuators A: Phys, 268 (2017), pp. 38-45.

[5] L. Lu, P. Guo, Y. Pan, **Magnetic-Field-Assisted projection stereolithography for three-dimensional printing of smart structures**, J. Manuf. Sci. E, 139 (2017), pp. 1008-1008-7.

[6] M. E. Fleet, **The structure of magnetite: symmetry of cubic spinels**, J. Solid State Chem., 62 (1986), pp. 75-82.

[7] F. Walz, **The Verwey transition-a topical** review, J. Phys. Condens. Matter, 14 (2002), R285-R340.

[8] R. Aragón, D. J. Buttery, J. P. Shepherd, J. M. Honig, **Influence of nonstoichiometry on the Verwey transition**, Phys. Rev. B, 31 (1985), pp. 430-436.

[9] M. Mikhaylova, D. K. Kim, N. Bobrysheva, M. Osmolowsky, V. Semenov, T. Tsakalakos, M. Muhammed, **Superparamagnetism of magnetite nanoparticles: dependence on surface modification**, Langmuir, 20 (2004), pp. 2472-2477.

[10] Y. Zhang, N. Kohler, M. Zhang, **Surface modification of superparamagnetic magnetite nanoparticles and their intracellular** uptake, Biomaterials, 23 (2002), pp. 1553-1561.

[11] J. Ge, Y. Hu, M. Biasini, W. P. Beyermann, Y. Yin, **Superparamagnetic magnetite colloidal nanocrystal** clusters, Angew. Chem. Int. Ed., 46 (2007), pp. 4342-4345.

[12] R. Cano, M. Yus, D. J. Ramón, **Impregnated copper or palladium-copper on magnetite as catalysts for the domino and stepwise Sonogashira-cyclization processes: a straightforward synthesis of benzo [b]furans and indoles**, Tetrahedron, 68 (2012), pp. 1393-1400.

[13] M. Muñoz, Z. M. de Pedro, J. A. Casas, J. J. Rodriguez, **Preparation of magnetite-based catalysts and their application in heterogeneous Fenton oxidation-a review**, Appl. Catal. B., 176 (2015), pp. 249-265.

[14] S. Mornet, S. Vasseur, F. Grasset, E. Duguet, **Magnetic nanoparticle design for medical diagnosis and therapy**, J. Mater. Chem., 14 (2004), pp. 2161-2175.

[15] T. D. Schladt, K. Schneider, H. Schild, W. Tremel, **Synthesis and bio-functionalization of magnetic nanoparticles for medical diagnosis and treatment**, Dalton Trans., 40 (2011), pp. 6315-6343.

[16] P. Tartaj, M. P. Morales, T. Gonzalez-Carreño, S. Veintemillas-Verdaguer, C. J. Serna, **The iron oxides strike back: from biomedical applications to energy storage devices and photoelectrochemical water splitting**, Adv. Mater., 23 (2011), pp. 5243-5249.

[17] Q. Q. Xiong, J. P. Tu, Y. Lu, J. Chen, Y. X. Yu, Y. Q. Qiao, X. L. Wang, C. D. Gu, **Synthesis of hierarchical hollow-structured single-crystalline magnetite (Fe3O4) microspheres: the highly powerful storage versus lithium as an anode for ion batteris**, J. Phys. Chem. C., 116 (2012), pp. 6495-6502.

[18] C. E. Diebel, R. Proksch, C. R. Green, P. Neilson, M. M. Walker, **Magnetite defines a vertebrate magnetoreceptor,** Nature., 40 (2000), pp. 299-302.

[19] R. B. Frankel, R. P. Blakemore, R. S. Wolfe, **Magnetite is freshwater magnetotactic bacteria,** Science, 20 (1979), pp. 1355-1356.

[20] J. L. Kirschvink, A. Kobayashi-Kirschvink, B. J. Woodford, *Proceedings of the National Academy of Sciencies,* 1992, **89(16)**, 7683-7687.

[21] M. A. Martínez Banaclocha, I. Bókkon, H. Martínez Banaclocha, **Magnetic biomaterialization in the human brain**, Med. Hypotheses, 74 (2010), pp. 254-257.

[22] M. Thakur, K. De, S. Giri, S. Si, A. Kotal, T. K. Mandal, **Interparticle interaction and size effect in polymer coated magnetite nanoparticles**, J. Phys. Condens. Mater., 18 (2006), pp. 9093-9104.

[23] M. Wu, Y. Xiong, Z. Peng, N. Jiang, H. Qi, Q. Chen, **The enhanced coercivity for the magnetite/silica nanocomposite at room temperature**, Mater. Res. Bull., 39 (2004), pp. 1875-1880.

[24] V. V. Mody, A. Singh, B. Wesley, **Basics of magnetic nanoparticles for their application in the field of magnetic fluid hypothermia**, J. Nanomedicine, 5 (2013), pp. 11-21.

[25] J. A. Beamish, J. Zhu, K. Kottke-Marchant, R. E. Marchant, **The effects of monoacrylated poly(ethylene glycol) on the properties of poly (ethylene glycol) diacrylate hydrogels used for tissue engineering**, J. Biomed. Mater. Res. A.,92 (2010), pp. 441-450.

[26] R. Domingo-Roca, B. Tiller, J. C. Jackson, J. F. C. Windmill, **Bio-inspired 3D-printed piezoelectric device for acoustic frequency selection**, Sens. Actuators A: Phys., 271 (2018), 1-8.

[27] G. W. D. Spratt, P. R. Bissell, R. W. Chantrell, E. P. Wohlfarth, **Static and dynamic experimental studies of particulate recording media**, J. Magn. Magn. Mater, 75 (1988), pp. 309-318.

[28] T. Thomson, K. O'Grady, **Magnetization reversal mechanisms and time-dependent processes in Tb-Fe-Co alloy films**, J. Phys.: Appl. Phys., 30 (1997), pp. 1566-1575.

[29] T. Thomson, K. O'grady, G. Bayreuther, **Magnetization reversal mechanisms and time-dependent processes in thin Tb/Fe multilayer films**, J. Phys. D: Appl. Phys*,* 30 *(*1997), pp. 1577-1587.

[30] P. R. Bissell, M. Cerchez, L. Stoleriu, R. W. Chantrell, A. Stancu, **The use of ΔM plots in the magnetic characterization of particulate media**, J. Magn. Magn. Mater., 266 (2003), pp. 1-7.

[31] C. P. Bean, J. D. Livingston, **Superparamagnetism**, J. Appl. Phys., 30 (1959), pp. S120-S129.

[32] F. C. Fonseca, G. F. Goya, R. F. Jardim, R. Muccillo, N. L. V. Carreno, E. I. Longo, E. R. Leite, **Superparamagnetism anfd magnetic properties of Ni nanoparticles embedded in SiO2**, Phys. Rev. B, 66 (2002), pp. 104406-1 – 104406-5.

[33] B. Kalska, J. J. Paggel, P. Fumagalli, **Magneto-optics of thin magnetic films composed of Co nanoparticles**, J. Appl. Phys., 92 (2002), pp. 7481-7485.

[34] Y. Sato, J. Furukawa, **A molecular theory of filler reinforcement based upon the conception of internal deformation (a rough approximation of the internal deformation)**, Rubber Chem. Technol., 36 (1963), pp. 1081-1106.

[35] C. Credi, A. Fiorese, M. Tironi, R. Bernasconi, L. Magagnin, M. Levi, S. Turri, **3D printing of cantilever-type microstructures by stereolithography of ferromagnetic photopolymers**, ACS Appl. Mater. Interfaces, 8 (2016), pp. 26332-26342.

[36] Y. Zare, Study of nanoparticles aggregation/agglomeration in polymer particulate nanocomposites by mechanical properties, Composites: Part A, 84 (2016), pp. 158-164.

Supplementary material

Table I: Values of the mass, magnetisation of saturation (M_s), coercive field (H_c), and relative permeability (μ_r) of all the synthesized samples. The number in brackets corresponds to the wt% of magnetic NPs.

Sample	m [mg]	M_s [emu/g]	H_c [Oe]	μ_r
Fe(50)@Irg;BEMA	3.3	100	16	2.44
Fe(50)@Irg;PEGDA	5.1	124	16	1.60
Fe(50)@PhI;BEMA	4.5	87	17	2.00
Fe(75)@Irg;PEGDA	3.8	167	15	3.08
Fe_3O_4(25)@Irg;BEMA	4.1	23	107	1.60
Fe_3O_4(50)@Irg;BEMA	3.9	46	105	2.23
Fe_3O_4(50)@Irg;PEGDA	4.3	50	105	2.51
Fe_3O_4(50)@PhI;BEMA	4.0	46	104	2.24
Hybrid	5.4	66	74	2.06

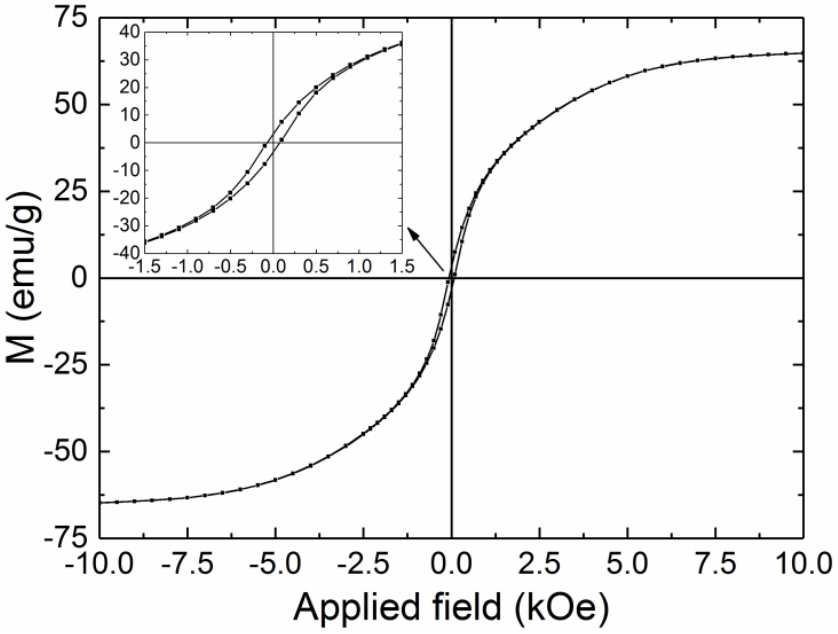

Fig. 11: Hysteresis loop of the hybrid magnetic composite material, composed by several layers of Fe(50 wt%)@Irg819+BEMA, and Fe_3O_4(50 wt%)@Irg819+BEMA. The top-left corner graph shows a close-up look at the low-field regime in which the ferromagnetic behaviour of the sample can be observed.

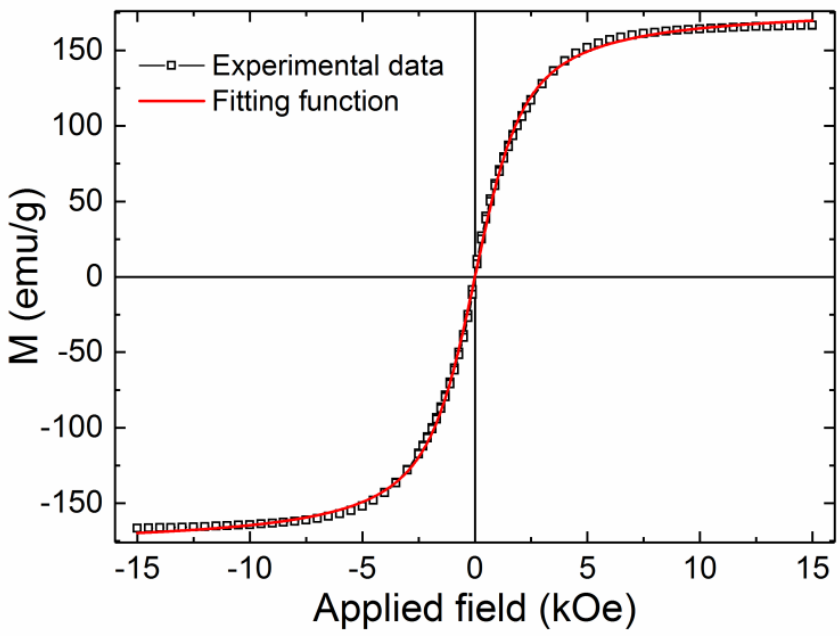

Fig. 12: Fitting of the *M-H* curve of one of the Fe composites using the Langevin function, Eq. (3). The empty squares show the experimental data and the continuous red line shows the fitting function.

Table II: NPs sizes determined from the *M-H* plots using the Langevin function, given by Eq. (3) in the main text. Two sizes were determined for each sample in which the experimental and the fitting M_s values were used.

Sample	M_s [emu/g]	NP size [nm]
Fe(50)@Irg;BEMA	100	4.076
	110	3.95
Fe(50)@Irg;PEGDA	124	2.23
	135	2.17
Fe(50)@PhI;BEMA	87	2.14
	99	2.047
Fe(75)@Irg;PEGDA	167	2.10
	180	2.042
Fe_3O_4(25)@Irg;BEMA	23	10.84
	24	10.72
Fe_3O_4(50)@Irg;BEMA	46	8.88
	48	8.79
Fe_3O_4(50)@Irg;PEGDA	50	8.95
	51	8.87
Fe_3O_4(50)@PhI;BEMA	46	8.87
	48	8.77